Effect of Active Camber on Rotor Noise, Power and Hub Vibration

Sumeet Kumar*, Dominik Komp†, Manfred Hajek‡
Institute of Helicopter Technology, Technical University of Munich, Munich 85748, Germany

Jürgen Rauleder§
Georgia Institute of Technology, Atlanta, GA 30332, USA

This paper presents a computational study that was conducted to investigate the impact of active-camber actuation on an isolated full-scale Bo 105 rotor for noise, power consumption and (non-rotating) hub vibration. The study was carried out at advance ratios μ=0.05–0.35 using CAMRAD II based comprehensive analysis for the rotor aeromechanics. Acoustic analysis was carried out using the Ffowcs Williams–Hawkings equation formulation for elastic blades using PSU-WOPWOP. To automate the generation of compliant data files and the subsequent analysis, an open-source post-processing framework was created. The active-camber actuation scheduling and amplitude were varied at each advance ratio and significant effects on rotor acoustics, rotor power, and induced hub vibration were obtained. Using 1P (once-per-revolution) and 2P active-camber actuation, it is shown that low advance ratios μ=0.05–0.15 were more amenable to simultaneous reduction of power and hub vibration. For advance ratios of μ=0.10 and 0.15, simultaneous reduction of rotor noise, power, and hub vibration was obtained. Based on the results of a separate larger parametric study at advance ratio μ=0.30, it was found that the same physical effects that led to power reduction also resulted in rotor noise reduction by up to 15 dB below the rotor plane.

I. Nomenclature

A_{mP}	=	active-camber deflection amplitude of m-th harmonic component, deg
C_d	=	blade drag coefficient
C_H	=	rotor drag force coefficient (shaft axis)
C_l	=	blade lift coefficient
C_P	=	coefficient of power
C_T	=	rotor thrust coefficient (shaft axis)
c	=	blade chord, m
F_{4X}	=	Non-rotating 4/rev longitudinal hub shear force, N
F_{4Y}	=	Non-rotating 4/rev lateral hub shear force, N
F_{4Z}	=	Non-rotating 4/rev vertical shear force, N
J	=	rotor hub vibration index
l_r	=	force per-unit-area acting (due to surface element) on the fluid in the direction of observer
M	=	Mach number
M_r	=	source Mach number in the direction of the observer
M_{4X}	=	Non-rotating 4/rev hub roll moment, Nm
M_{4Y}	=	Non-rotating 4/rev hub pitching moment, Nm
M_{4Z}	=	Non-rotating 4/rev hub yaw moment, Nm
n	=	active control input harmonic, 1/rev
OASPL-A	=	A-weighted overall sound pressure level, dB
p'	=	acoustic pressure, Pa

*Graduate Research Assistant, sumeet.kumar@tum.de
†Graduate Research Assistant, dominik.komp@tum.de
‡Professor and Department Head, hajek@tum.de
§Assistant Professor, Daniel Guggenheim School of Aerospace Engineering, juergen.rauleder@gatech.edu, Senior Member AIAA

p'_{far}	=	far-field acoustic pressure, Pa
R	=	rotor blade radius, m
r	=	distance between the observer and the source, $r = \|\mathbf{x} - \mathbf{y}\|$
r_0	=	radial position of the active-camber section center, normalized by rotor radius
s	=	radial span of the active-camber section, normalized by rotor radius
t	=	observer time, s
v_n	=	local velocity of surface element in the locally normal direction, m/s
α_s	=	rotor shaft tilt (negative forward), deg
δ	=	active-camber deflection (positive downwards), deg
δ_0	=	constant active-camber deflection component in δ, deg
τ	=	source (blade surface element) time, s
σ	=	rotor solidity
ϕ_{mP}	=	active control input phase lag of m-th harmonic component, deg
ψ	=	rotor azimuth angle,deg

II. Introduction

DUE to their ability to take-off and land vertically, helicopters occupy a niche utility purpose for use in the military as well as civilian applications. Reducing helicopter noise has clear tactical advantages for military applications. Given that civilian applications involve helicopters operating over cities, greater community acceptance is likely if quieter operation could be ensured. Ongoing industry excitement and intrigue over eVTOLs, as a ubiquitous mode of intra-city transport, has only brought on additional scrutiny to the noise generated by lifting rotors.

The assymetrical aerodynamic conditions due to edgewise rotor flight bring with it an assortment of design challenges that impose physical performance limitations in forward flight. Due to the low dynamic pressure on the retreating side, the one-per revolution design feature imposed by the swashplate on blade pitch ensures a high blade pitch on the retreating side to maximize lift generation. However, this usually leads to low blade pitch on the advancing side so that the outboard sections of the blade sometimes end up producing negative lift. This helps avoid large positive roll moments and maintain steady flight trim, but ultimately makes the overall rotor less efficient.

At normal cruise flight conditions, helicopter main rotor noise is primarily due to displacement of the air due to finite thickness of the airfoils section and due to pressure perturbations from blade airloads. The former is referred to as the thickness noise and the latter as the loading noise.The relative magnitudes of the two components in total rotor noise depends not only on the operational state of the main rotor but also the position relative to the rotor. While noise does decrease with distance, the directivity of the thickness noise is largely in the plane of the rotor disk and decreases rapidly with elevation angle away from the rotor plane. Loading noise, composed of noise due to blade drag as well as lift, is directed along directions in which these forces act. So, loading noise has an in-plane directivity component due to blade drag forces which are much smaller compared to the lifting forces and as a result the directivity is largely in the out-of-plane direction i.e. the direction of lifting forces.

Based on this understanding of the rotor noise generating mechanisms, several passive techniques have been explored in the past, to reduce rotor noise. In [1], a double swept blade design targeted at reducing blade noise is discussed. The acoustic benefits of a novel rotor with modulated blade spacing are shown in [2]. The motivation behind the investigation was to spread the rotor acoustic energy over a wider spectrum compared to a uniformly spaced rotor. While some improvements in rotor acoustics were shown in that analytical study, significant performance losses arising from rotor blades with uneven spacing were reported. While not reported in that study, it is expected that the rotor hub vibration resulting due to uneven blade spacing would have to be critically examined as well. Subjective tests on participants performed in a companion study [3], using digitally altered audio signals, failed to corroborate the acoustic benefits of uneven blade spacing. Using a simple analytical approach in [4] the potential of 'X-force' or longitudinal force controllers was shown to influence the tip-path plane of the rotor disk during descent approaches and avoid rotor noise due to blade-vortex interaction.

During normal cruise flight conditions, the highest acoustic noise is generated in the plane of the rotor, with the blade thickness noise being the major contributing component. Gopalan and Schmitz [5] conducted the first theoretical study of its kind, exploring the possibility of reducing helicopter thickness noise by generating 'anti-noise' pulses using on-blade active controls. Full-scale rotor experiments in [6] using on-blade control have reported reduction of low-frequency in-plane rotor noise by exploiting essentially the same physics as laid out in [5]. Optimization strategies are presented in [7] to obtain optimal on-blade loading solution that minimizes the rotor noise over a range of the rotor

azimuth instead of just minimizing it for a single observer. The study, however, did not account for the loading due to the baseline rotor and just used the delta loading input due to the on-blade active mechanism in its formulation for the loading noise component. Since active blade actuation can significantly affect the baseline trim state of the rotor, it appears necessary to include the effect of the overall blade loading for a more accurate solution. The effect of active actuation on blade thickness noise, due to changing section profile, needs to be included as well.

Within the scope of the EU-funded project **SABRE** (**S**hape **A**daptive **B**lades for **R**otorcraft **E**fficiency), an active-camber mechanism installed on rotor blades is envisaged to improve rotor performance through power savings, as well as to reduce noise emissions. Previous studies conducted in this context [8, 9] have shown the potential of the blade morphing mechanism to reduce required rotor power by up to 4.4% when actuated dynamically during cruise forward flight ($\mu = 0.3$) as well as to reduce non-rotating vibratory hub loads. In the current study, the scope of investigation was expanded to advance ratios of $\mu = 0.05 - 0.35$ and active actuations were considered at 1P and 2P for a range of actuation amplitudes and input phase angles, i.e. the actuation scheduling was varied over the rotor disk. The current investigation into the ability of active on-blade mechanisms to reduce rotor noise and power consumption also includes hub vibration for a more practical all-round assessment of these mechanisms since higher harmonic actuation of lifting devices has the potential to impact vibratory hub loads.

III. Modeling Approach

The current investigation was carried out using results obtained from aeromechanics analysis of an isolated Bo 105 rotor. The comprehensive analysis code CAMRAD II (CII) [10] was used to obtain distributed trimmed rotor blade forces and elastic deformations for the baseline rotor as well as the for active morphing rotor. The acoustic solver PSU-WOPWOP [11] was used to estimate the rotor noise using the results obtained from CII analyses. The study involved a sweep of advance ratios of $\mu = 0.05 - 0.35$ at slightly different trim conditions for each advance ratio. These are detailed below in Table 1. The following provides details regarding the comprehensive analysis model, the acoustic analysis model, and the post-processing framework created to streamline the entire investigation.

Table 1 Trim conditions

μ	α_s(°)	C_T/σ	M_x (Nm)	C_H/σ
0.05	-1	0.0886	1000	-0.00023
0.10	-2	0.0886	600	-0.00093
0.15	-3	0.0886	500	-0.00210
0.20	-4	0.0886	600	-0.00370
0.25	-5	0.0886	700	-0.00580
0.30	-6	0.0886	1000	-0.00840
0.35	-7.3	0.0886	1400	-0.01150

A. Comprehensive Rotor Aeromechanics Model

The current study was based on an isolated full-scale Bo 105 rotor model including a swashplate mechanism. Radially distributed structural properties of the blade were provided by DLR. The elastic blade motion was calculated using elastic beam theory. The deflection of the active-camber section was prescribed and inertial effects due to dynamic actuation as well as chordwise section deformation were not considered. The blade aeordynamics were calculated using lifting-line theory based on 2-D airfoil polars that were generated using RANS-based CFD simulations [12]. All analyses were carried out using 24 time steps per revolution, i.e., an azimuthal step size of 15°. For the aerodynamics, a different azimuthal step size was adopted and this is addressed later. Past investigation in [6] deemed such an azimuthal resolution adequate for low-frequency acoustics investigations, but results from a sensitivity study are presented later to confirm this finding. Further details about the aeromechanics model can be obtained from [8] where the baseline model was validated using full-scale rotor wind tunnel measurement data at $\mu = 0.3$, and rotor power and trim angles were compared for an advance ratio sweep. Further results validating the model with flight test data at different advance ratios are presented in [13] .

Figure 1 provides details of the active-camber morphing mechanism as well as the blade integration model used for

the analysis. Figure 1(a) shows a model-scale test setup of the mechanism under-development. Figure 1(b) specifies the trailing-edge defoection angle δ, as measured from 75%c, as the metric for measuring the camber deflection. The baseline (non-morphing) airfoil was a NACA23012. The front 75% of the morphing section was equivalent to the NACA23012 baseline airfoil, and only the aft 25%c was continuously deformed. This was a good compromise between aerodynamic efficiency and structural feasibility. The baseline airfoil chord was used as the reference to measure the angle of attack irrespective of the degree of camber deflection. For example, all airfoil shapes shown in Fig. 1(b) are at the same angle of attack. Based on a results obtained in a previous study investigating rotor performance improvement with active-camber actuation [14], the active-camber mechanism was implemented on the blade with $r_0 = 0.7$ and $s = 0.4$ (see Fig. 1(c)). Such a configuration was found to be most efficient in terms of rotor performance improvement. The camber deflection was defined as a superposition of harmonic inputs following Eq. (1). δ_0 is the mean deflection amplitude, and A_{mP} and ϕ_{mP} are the amplitude and phase difference, respectively, of the mth harmonic component of the active-camber input. Table 2 provides details of the amplitudes for which a parametric phase angle sweep was carried out to investigate the effect of active-camber actuation on rotor noise emissions, performance, and hub vibration. In addition to the quantities shown in Table 2, δ_0 was taken to be [0°,1°,2°,3°], bringing the combination of cases investigated to be around 300 for each advance ratio and each actuation frequency.

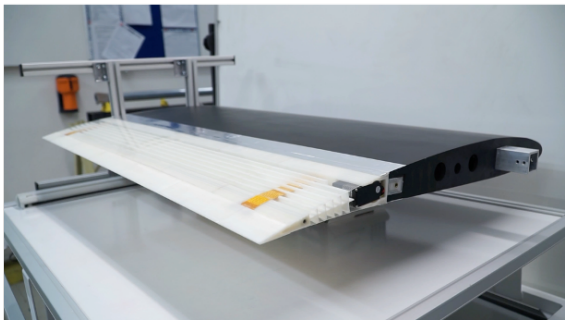

(a) Model cross-section with camber morphing (courtesy of University of Bristol)

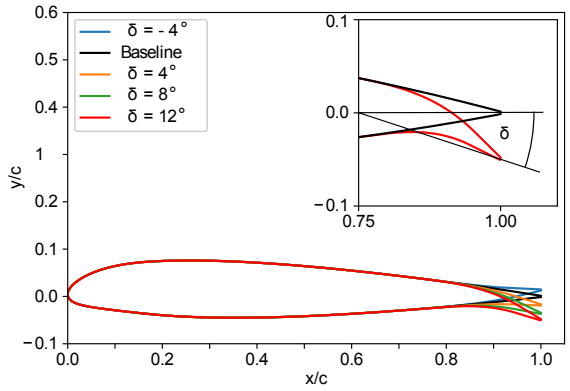

(b) Illustration of the details of the morphing cross-section (adapted from [14])

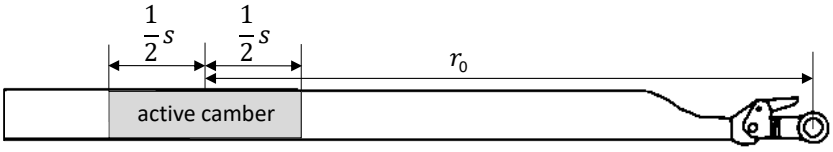

(c) Installation of active morphing section on a blade (adapted from [14])

Fig. 1 Details of the active-camber morphing mechanism layout and on-blade installation.

$$\delta = \delta_0 + \sum_m A_{\mathrm{mP}} \cdot \cos(m\psi - \phi_{\mathrm{mP}}) \tag{1}$$

Table 2 Active-camber parametric study.

Actuation freq	Phase	Phase-stepping	Amplitude
m	ϕ_{mP}	$\Delta\phi_{\mathrm{mP}}$	A_{mP}
0P	-	-	[0°,1°,2°,3°]
1P	0°-360°	30°	[0.25°,0.5°,1.0°,1.5°,2.0°,2.5°,3.0°]
2P	0°-360°	30°	[0.25°,0.5°,0.75°,1.0°,1.25°,1.5°]

B. Acoustics Analysis

The rotor noise prediction code PSU-WOPWOP, developed at PennState University by Prof. Kenneth Brentner and his students, was used to predict the rotor acoustic noise in the present study. The theoretical basis of the code is the Eq. 2 proposed by Ffowcs Williams and Hawkings (FW-H) which is an exact rearrangement of the Navier-Stokes (NS) equations for arbitrarily moving surfaces. Since the FW-H equation is essentially a rearrangment of the NS equations, solving it over the flow domain is no easier than the NS equations themselves. It is formulated in generalized function space so that it becomes valid in unbounded space. This makes it amenable to solve using the free-space Green's function. One such integral solution in time and space was proposed in [15] and is referred to as Formulation 1A (Eq. 3).

$$\frac{1}{c^2}\frac{\partial^2 p'}{\partial t^2} - \nabla^2 p' = \underbrace{\frac{\partial}{\partial t}\left[\rho_o v_n \delta\left(f\right)\right]}_{\text{monopole source term}} - \underbrace{\frac{\partial}{\partial x_i}\left[l_i \delta\left(f\right)\right]}_{\text{dipole source term}} + \underbrace{\frac{\partial^2}{\partial x_i x_j}\left[T_{ij} H\left(f\right)\right]}_{\text{quadrupole source term}} \tag{2}$$

$$\begin{aligned} 4\pi p'(\mathbf{x},t) = & \underbrace{\int_{f=0}\left[\frac{\rho_o\left(\dot{v}_n + v_n\right)}{r(1-M_r)^2} + \frac{\rho_o v_n\left(r\dot{M}_r + c\left(M_r - M^2\right)\right)}{r^2(1-M_r)^3}\right]_\tau dS}_{\text{monopole source term (thickness noise)}} \\ & + \frac{1}{c}\underbrace{\int_{f=0}\left[\frac{\dot{l}_r}{r\left(1-M_r\right)^2} + \frac{l_r - l_M}{r^2\left(1-M_r\right)^2} + \frac{l_r\left(r\dot{M}_r + c\left(M_r - M^2\right)\right)}{r^2\left(1-M_r\right)^3}\right]_\tau dS}_{\text{dipole source term (loading noise)}} \end{aligned} \tag{3}$$

Here, an integration is carried out over the impermeable surface responsible for perturbing the flow, i.e. the rotor blade, by evaluating the relevant quantities at source time τ. The subscripts n and r correspond to the vector directions normal to the surface f (i.e., the blade surface over which the surface integral is evaluated), the radial direction between the surface grid cell and the observer, respectively. The parameters ρ_0 and c refer to the quiescent flow properties - flow density and the speed of sound. v is the surface grid velocity, M is the Mach number, and l is the loading force acting on the fluid due to the surface element dS.

In Eq. 3, the total acoustic pressure perturbation is ascribed to physically relevant attributes such as the lifting-surface geometry (thickness noise) and the blade airloads (loading noise). In the absence of high-speed impulsive noise, i.e., if the Mach number at any blade section is below 0.9 [16], the quadrupole-like source term in Eq. 2 is usually dropped and Eq. 3 can be used to predict rotor noise fairly accurately. It has become standard practice to predict rotor noise, and particularly helicopter main rotor noise, using this procedure since it allows using details of the blade geometry and blade airloads to predict rotor noise fairly accurately.

The acoustic analysis in itself is computationally fast, on the order of one second per blade and observer location (using lifting-line aerodynamics and medium blade surface discretization resolution). The blade airloads could be obtained from lifting-line based or blade element momentum theory based comprehensive analyses, or using CFD simulations. The premise is that the more accurately the source terms on the right hand side of Eq. 3 are modeled, the more accurate is the predicted acoustic pressure fluctuation. However, this is valid only when the quadrupole-like term of Eq. 2, that was dropped in Eq. 3, is comparably lower than the other two source terms. This happens for flight conditions where the blade tip approaches the delocalization Mach number, so named because the transonic flow due to high blade tip speed causes shock waves to appear that detach from the blade and lead to much higher noise than that predicted just using the monopole and dipole contributions. For the maximum advance ratio of $\mu = 0.35$ investigated in this study, the advancing blade tip Mach number does not exceed 0.86. Given that the NACA23012 is a 12% thick airfoil, it is reasonable to assume that no shocks occur throughout the investigated flight regime and that acoustic predictions based on Eq. 3 are physical.

C. Post-Processing Framework

As is evident from Eq. 3, the acoustic pressure disturbance due to the lifting surface under investigation is obtained via a surface integration of relevant flow and aerodynamic quantities. These quantities can be obtained from either CFD simulations or from lifting-line based analyses. Surface discretization is inherent to CFD simulations and the same can be used as is within the framework of acoustic analysis. However, rotor comprehensive analyses generally use a lifting-line representation of the blade aerodynamics and a 1-D beam representation for structural analysis. So,

a geometric discretization of the lifting surface is not inherent to comprehensive analyses and needs to be generated separately. For the current study, involving analyses based on CII output results, a framework was created for generating a structured surface grid based on blade geometry data. For this purpose, the existing functionalities available for blade surface generation within the in-house open source multidisciplinary blade design and optimization tool SONATA [17] were leveraged and the framework was built on top of it. This also ensures a possibility for future incorporation of acoustic footprint as an objective within blade design optimization. The blade geometry definition is provided as a YAML file. It contains information such as the airfoil profile, chord length, reference location, blade pitch etc. at each spanwise location to generate the blade surface geometry with high accuracy. Based on this information, and the custom methods introduced in SONATA to generate the lifting surface geometry for the purpose of acoustic analysis, a rigid blade geometry can be generated.

The elastic blade deformation is obtained from the trimmed rotor CII output file at each blade section as a set of 3 displacements and 3 rotations, at each time step. These are combined with the rigid blade definition to obtain the elastic blade surface definition and stored as a binary file, called a 'patch' file, in a format specific to PSU-WOPWOP [18]. The blade forces are obtained from CII solution file in the local blade Cartesian frame and are stored without modification in a binary format within a 'functional' data file. The above process of generating the surface geometry and loading files, illustrated in Fig. 2, can be extended to other comprehensive analysis codes (for e.g. Dymore [19]) if blade forces information at each time step is available as the output of the trimmed rotor solution. While the current study focuses on acoustic analysis based on results obtained using CII, it is envisaged that the final toolchain would be coupled with Dymore as well as CFD solver TAU [20]. Figure 3 illustrates this envisaged complete toolchain. Once the surface geometry and loading files are prepared, PSU-WOPWOP uses a 'namelist' file for providing further analysis specific inputs.

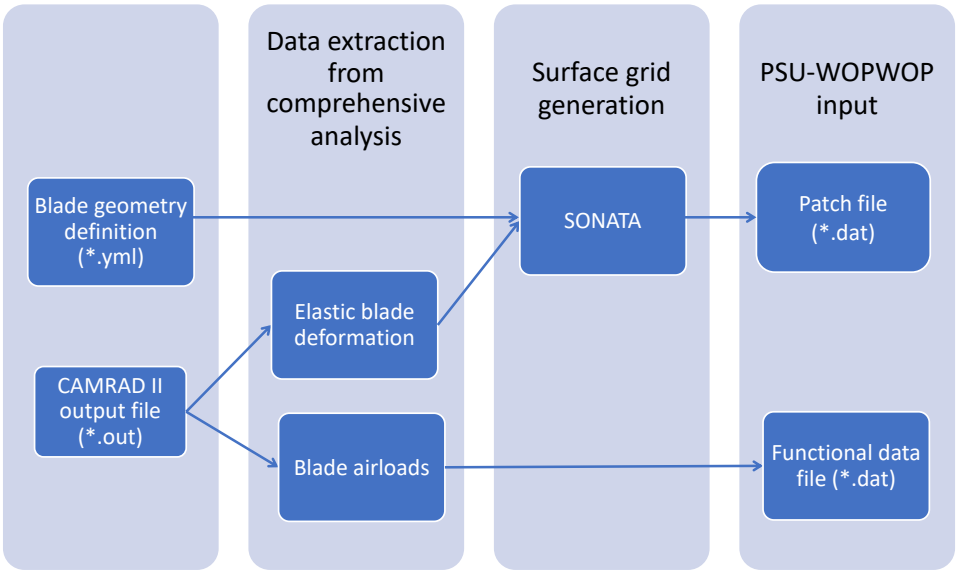

Fig. 2 Illustration of PSU-WOPWOP input file generation using CAMRAD II aeromechanics results.

Figure 4 shows the spanwise integration of the active-camber morphing section using the above framework and the corresponding surface discretization of the blade generated. An untwisted blade along with a high degree of camber morphing is shown in Fig. 4(a) to accentuate the transition region between the non-morphing and the morphing blade sections. For acoustic modeling purposes a linear transition region of 0.02R on either ends was assumed while the aerodynamic analysis model did not include any transition region. Figure 4(b) shows the geometry of the modeled elastic Bo 105 blade. Due to the low camber deflection angles involved in cases that showed potential to reduce rotor power, which are the focus of the current study, the morphing section or the transition regions are not discernible. Broadband noise is not modeled in the current study since it is usually relevant only for low RPM rotors [16]. The entire toolchain detailed above works seamlessly as long as the CII output file contains all the relevant blade airloads and corresponding elastic deformation data.

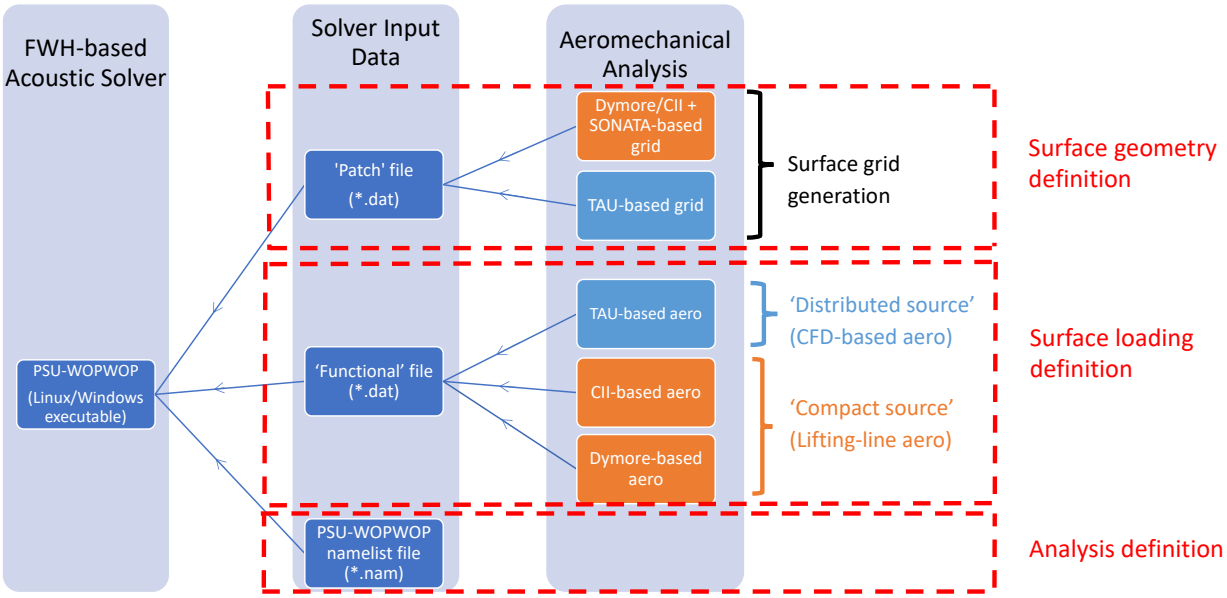

Fig. 3 Illustration of the rotor noise analysis toolchain.

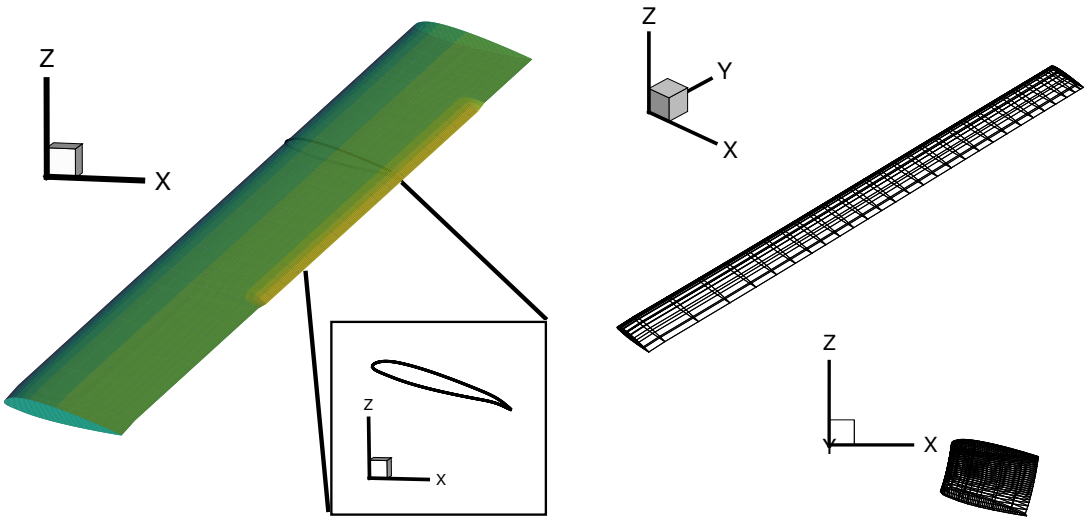

(a) Active camber on an example untwisted blade **(b) Bo 105 elastic blade surface discretization**

Fig. 4 Illustration of the generated morphing blade surface and discretization.

IV. Results and Discussion

The active rotor investigation was carried out for different actuation profiles (or scheduling) as dictated by parameters in Table 2 and Eq. 1. As a result, approximately 300 cases were investigated at each advance ratio for 1P and 2P, separately, since not all cases converged to a trimmed result. Rotor performance (i.e. power required), non-rotating hub vibration (4/rev component), and rotor acoustic footprint were analyzed for each of these cases within the parameter space investigated.

A. Rotor Performance and Hub Vibration

The non-dimensional rotor power coefficient, C_P, was used as a measure of the rotor power, and the non-dimensional hub vibration index J, defined in Eq. (4), was used as a measure of the rotor hub vibration. F_{4X0}, F_{4Y0} etc. refer to the baseline rotor 4P forces and moments, at a given advance ratio, that get transferred to the hub fixed frame from the rotating blades. F_{4X}, F_{4Y} etc. refer to the corresponding quantities for the active rotor. Designing a vibration measurement metric is a nuanced exercise that should take into account the relative sensitivity of human discomfort to forcing in different directions and varies with the investigated location within the fuselage [21]. However, Eq. (4) was chosen in the current study as the focus was to investigate the effect on 4P non-rotating hub forces and moments only as a first step towards reducing forces transferred from the rotor to the fuselage.

$$J = \sqrt{\left(\frac{F_{4X}}{F_{4X0}}\right)^2 + \left(\frac{F_{4Y}}{F_{4Y0}}\right)^2 + \left(\frac{F_{4Z}}{F_{4Z0}}\right)^2 + \left(\frac{M_{4X}}{M_{4X0}}\right)^2 + \left(\frac{M_{4Y}}{M_{4Y0}}\right)^2 + \left(\frac{M_{4Z}}{M_{4Z0}}\right)^2} \tag{4}$$

Figure 5 shows the effect of 2P harmonic actuation of the morphing camber section on rotor C_P and index J. Since J (Eq. 4) is non-dimensionalised, the corresponding value for the baseline rotor at each advance ratio is constant at $\sqrt{6}$. Within the parameter space of the current study (see Table 1), progressively fewer cases show reduced C_P with increase in advance ratio. This is because at low μ cases, non-zero δ_0 component in the deflection profile led to lower C_P for a larger range of ϕ_{mP}. It is evident from Fig. 5 is that C_P and J can separately be reduced at any forward flight speed but both appear to only be reduced simultaneously for the low advance ratio cases $\mu = [0.05, 0.10, 0.15]$. These are data points that lie in the third quadrant formed by the lines showing the baseline vibration index J (vertical dashed line) and the baseline C_P (horizontal dashed line) i.e. they lie to the left of baseline J line and below baseline C_P line.

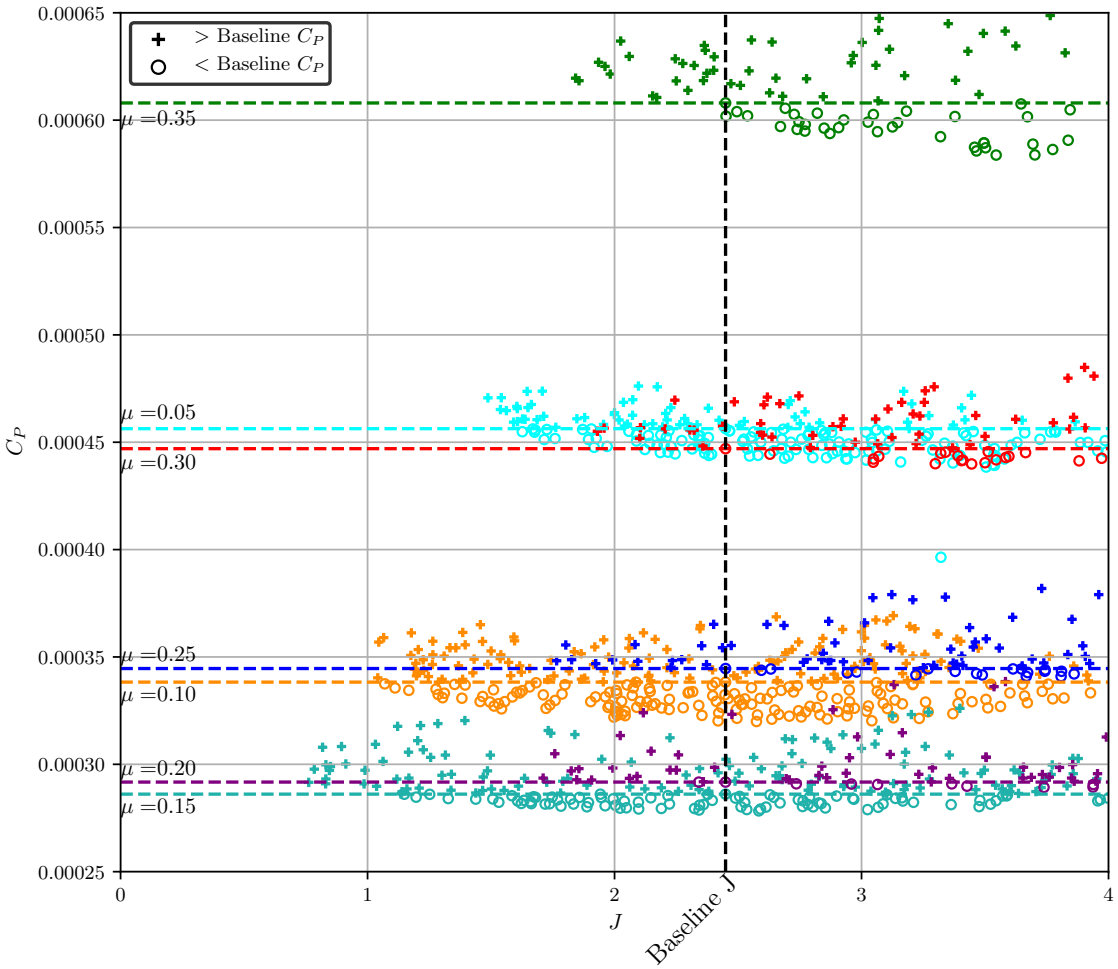

Fig. 5 Effect of 2P active-camber actuation on C_P and J at different advance ratios.

As has been discussed in detail in [8, 13], rotor performance improvement is a direct result of offloading sections of the rotor disk that are highly loaded. At high advance ratios the fore and aft sections are off-loaded and loading on the lateral sides is increased, in general. As a result, there are limited phase inputs ϕ_{mP} that can lead to this physical effect, and by extension improve rotor performance. For example, for 1P actuation performance improvement occurs when maximum camber deflection occurs around $\psi = 270^\circ$ and for 2P actuation frequency it occurs when maximum deflection is around $\psi = 0^\circ$ and $\psi = 180^\circ$.

The effect on J is the cumulative result of changes to F_{4X},F_{4Y},F_{4Z},M_{4X},M_{4Y} and M_{4Z}, and similar clustering of phase inputs ϕ_{mP} of relevant results does not occur. As mentioned above, for low advance ratios $\mu = [0.05, 0.10, 0.15]$ a constant camber deflection δ_0 is more beneficial towards reducing power consumption compared to a periodic variation since rotor aerodynamics has lower azimuthal assymetry at low advance ratios and the rotor disk is predominantly loaded over the blade tips. Increased lifting ability of the inboard blade sections due to a non-zero camber deflection component δ_0 helps reduce loading near the blade tips and blade sections there operate at higher C_l/C_d. As a result, a reduction in C_P is obtained at certain actuation amplitudes for all $\phi_{\text{mP}} = 0^\circ - 360^\circ$ for non-zero δ_0. Since performance improvement is then ensured for an entire phase range many more cases exhibit J lower than baseline case and appear in the respective third quadrant in Fig. 5. Qualitatively, similar trends exist for the 1P actuation cases as well except that at $\mu = 0.35$ a few cases exhibited simultaneous reduction in vibration and power. 1P results are not presented here for conciseness.

B. Rotor Acoustics

To obtain the effect of active-camber actuation on the footprint of rotor noise, i.e. directivity and magnitude, the total rotor noise was calculated at several locations placed on a hemispherical front that was centered at the rotor hub and moved with it (Fig. 6). Based on the relative acoustic effect of changes in sectional blade geometry, and aerodynamic drag and lift due to morphing, the maximum change in rotor noise could be effected differently for different observers over the hemisphere. Three locations, viz. A, B, and C, where chosen such that they are roughly in-plane, out-of-plane and below the rotor disk. Although less conspicuous in Fig. 6, the rotor shaft axis is tilted with respect to the plane of the hemisphere by the s

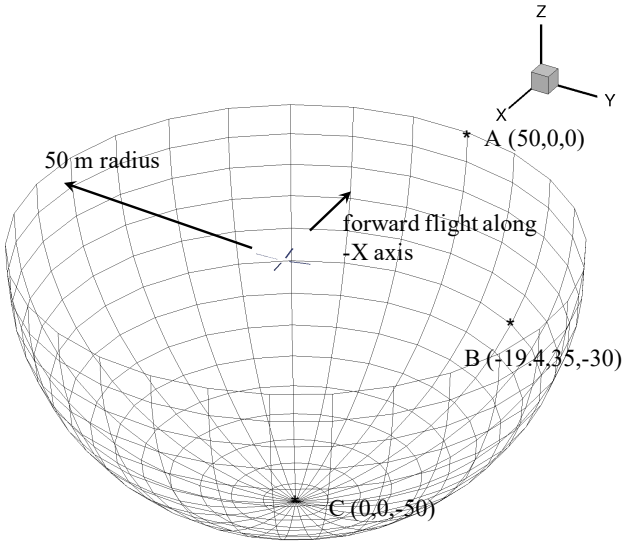

Fig. 6 Illustration of the arrangement of observers over a hemisphere below the rotor.

Due to the physiology of the human ear, tonal noise at the same sound pressure level can be perceived to have different loudness [22]. Sensitivity is high between frequencies 1000 Hz to 6000 Hz and drops off outside this range. So, a widely used measure of weighting the frequency spectrum, called A-weighted overall sound pressure level (OASPL-A) was used as a metric for comparing acoustic noise. The atmospheric density and the speed of sound were assumed to be based on the international standard atmospheric conditions (ISA). Figure 7 compares the baseline rotor noise using a relatively coarse resolution aerodynamic computation involving 24 steps over the rotor azimuth ($\Delta\psi = 15^\circ$), a resolution of 72 time steps ($\Delta\psi = 5^\circ$), and an even finer resolution of 120 time steps ($\Delta\psi = 3^\circ$). The blade elastic deflection motion was only resolved to 24 time steps in all cases. The results are based on an advance ratio of $\mu = 0.15$ since it

is representative of a low speed condition that is likely to manifest blade loading fluctuation from close encounters with trailed blade vortices. While the contour plots of total noise present some differences based on the resolution of aerodynamics used, the corresponding blade airloads shown in Fig. 8 show virtually identical results between $\Delta\psi = 5°$ case and $\Delta\psi = 3°$ case. This was observed also for results at $\mu = 0.05$ and $\mu = 0.1$ since the trim conditions were adopted for the study specifically so that blade-vortex interaction was avoided. Therefore, the aerodynamics were resolved using $\Delta\psi = 5°$ throughout the study.

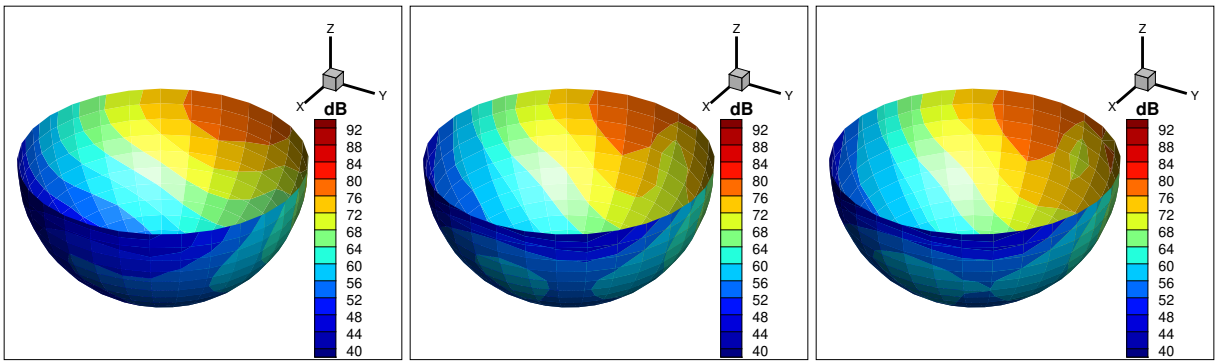

(a) $\Delta\psi = 15°$ **(b) $\Delta\psi = 5°$** **(c) $\Delta\psi = 3°$**

Fig. 7 OASPL-A contours of baseline rotor total noise at μ=0.15 for different resolutions of the aerodynamics analyses over a hemisphere 50 m from the rotor hub.

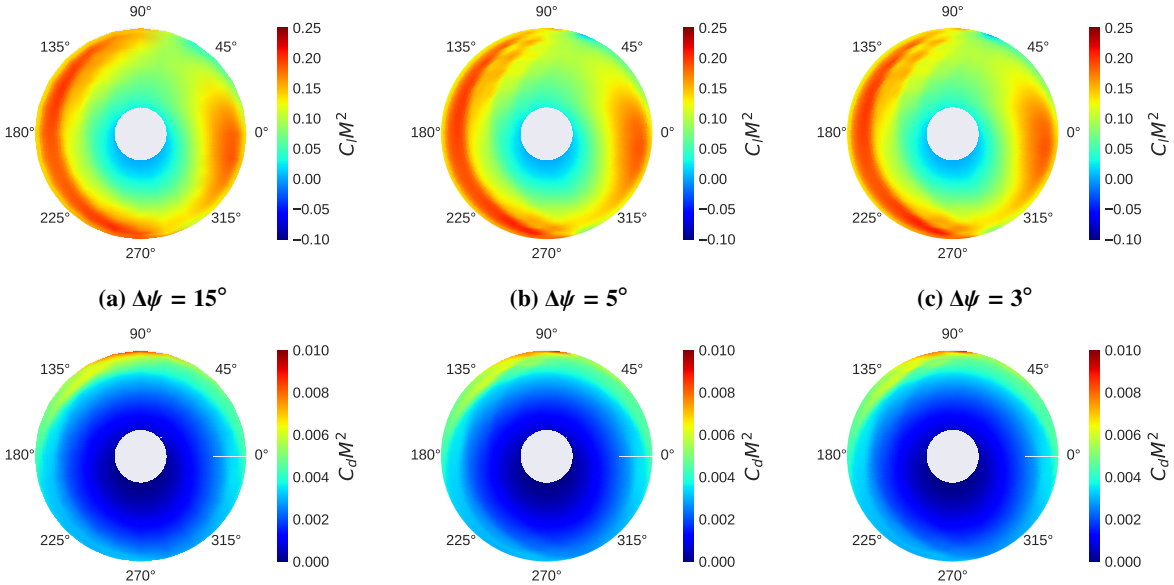

(a) $\Delta\psi = 15°$ **(b) $\Delta\psi = 5°$** **(c) $\Delta\psi = 3°$**

(d) $\Delta\psi = 15°$ **(e) $\Delta\psi = 5°$** **(f) $\Delta\psi = 3°$**

Fig. 8 Rotor lift and drag forces at μ=0.15 and different resolutions of aerodynamics analyses.

Figure 9 shows the rotor noise calculated at location B (see Fig. 6) versus change in rotor C_P. Only those results that showed a reduction in noise as well as power consumption have been shown for clarity. It can be observed that simultaneous reduction of total noise at location B and rotor power is possible throughout the advance ratio regime investigated. At $\mu = 0.05$, vibration reduction was obtained when peak camber deflection occurred in an azimuth range of 30° close to $\psi = 90°$ and 270° and this always led to higher noise at B. As a result, no case exhibited simultaneous reduction of all three quantities of interest.

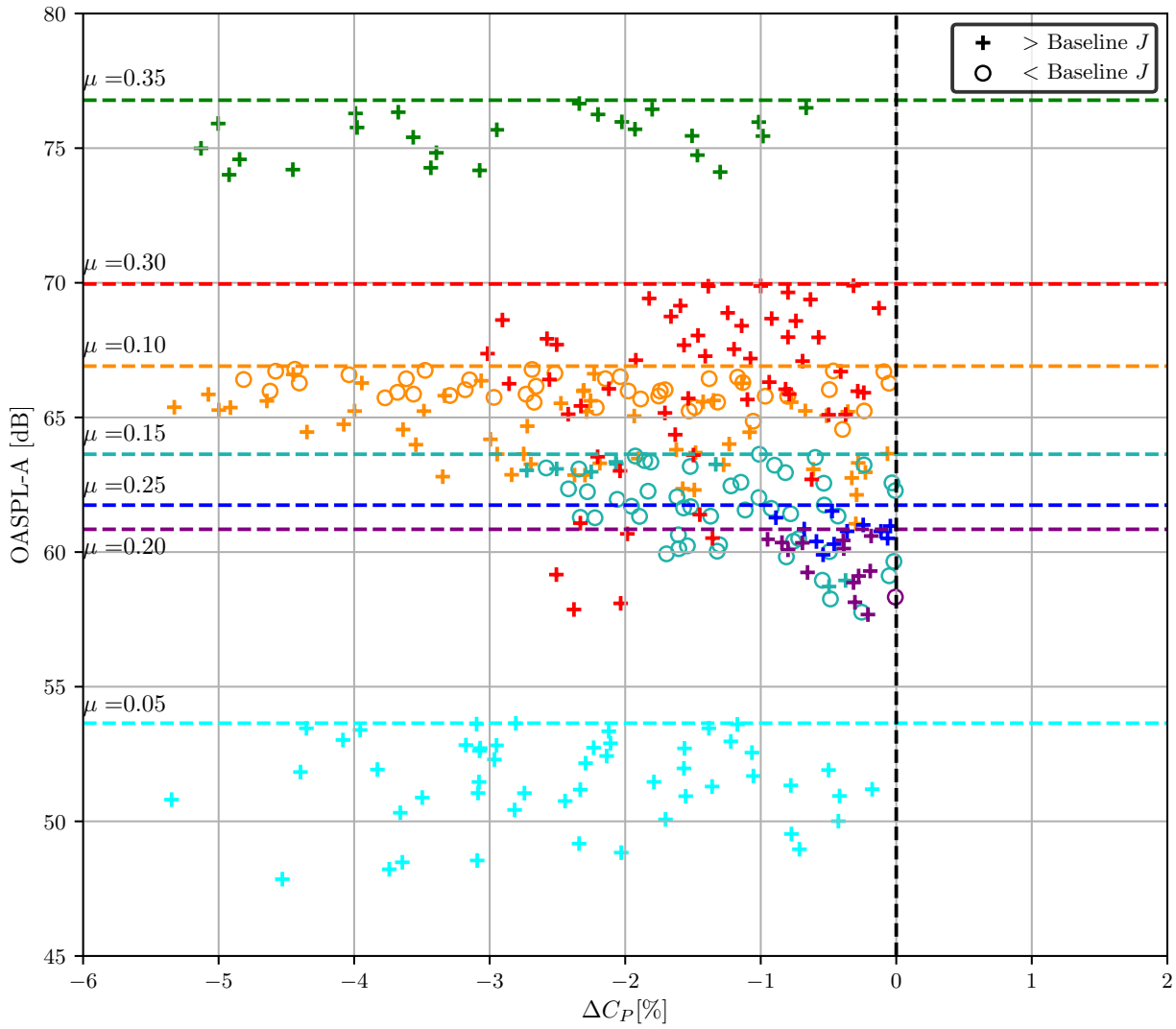

Fig. 9 Effect of 2P active-camber actuation on rotor OASPL-A at location B, C_P and J at different advance ratios. (For clarity, only cases with ΔC_P <0 and noise less than baseline rotor OASPL-A are shown.)

Figure 10 shows the active-camber deflection profiles over the azimuth for best performance cases using 1P, 2P and 1P+2P frequency components that were obtained after an extensive parametric study at an advance ratio of $\mu = 0.3$ as detailed in [8]. Note that for 2P actuation here, best performance was obtained for $r_0 = 0.75$ and $s = 0.30$ (see Fig. 1(c)). The following results discuss the corresponding rotor noise generated for these overall best performance cases from [8]. Figure 11 shows the acoustic footprint of the baseline case and 2P actuation case. The thickness noise directivity and magnitude remains largely unchanged since any changes in rotor tip-path-plane or geometry changes due to chordwise section deformation are not significant enough to affect thickness noise. Consequently, any change in total noise was a manifestation of variation in loading noise.

Rotor loading noise can be attributed to noise due to drag forces, which act primarily in the rotor plane, and that due to lifting forces, which act primarily out of the rotor plane. From Figs. 12(a)-(c) it can be observed that the directivity of loading noise due to in-plane forces is shifted azimuthally without affecting peak noise, but in Figs. 12d-f the magnitude of loading noise due to out-of-plane forces is reduced by 6 to 8 dB in the region of highest noise. Since noise in decibel is calculated on a logarithmic scale as the root mean square of pressure fluctuations, the total change in loading noise in Fig. 12(i) is not a superposition of the results in Figs. 12(c) and (f). The overall noise reduction occurs below the rotor

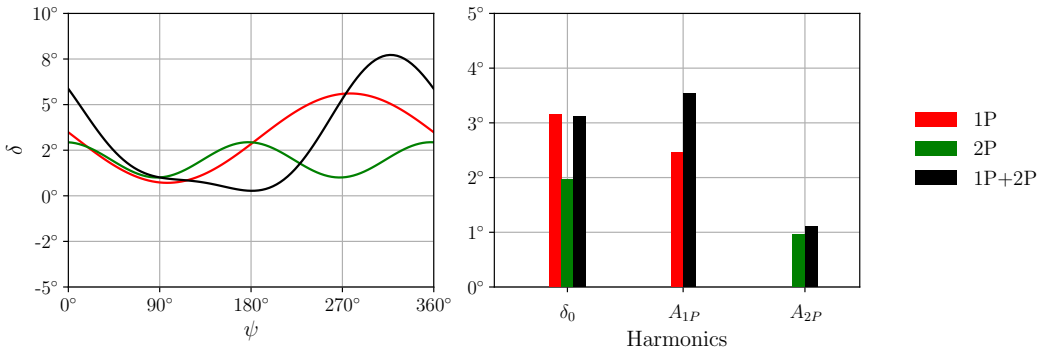

Fig. 10 Active-camber deflection profiles, and corresponding harmonic components, that lead to best rotor performance for 1P, 2P, and 1P+2P input at μ=0.3. (based on the study from [8])

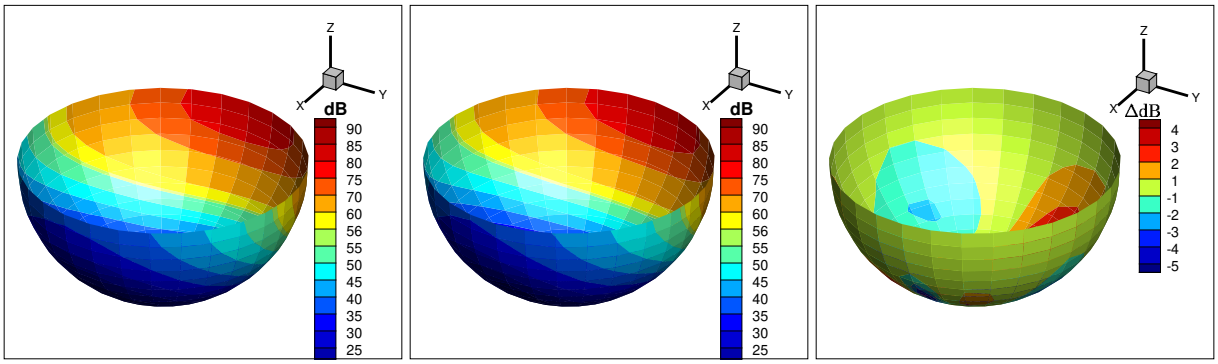

(a) Baseline **(b) 2P** **(c) Change in noise**

Fig. 11 OASPL-A contours of thickness noise for baseline rotor and 2P camber morphing case at μ=0.3 over a hemisphere of radius 50 m.

disk towards the front in the direction of forward flight. The change in directivity of loading noise (in-plane forces) can be attributed to change in rotor drag forces in the first quadrant compared to the baseline case (see Fig. 13). Since peak drag forces for 2P case occured close to $\psi = 90°$, the directivity of loading noise due to in-plane forces is directly ahead of the rotor at $\psi = 180°$ (Fig. 12(b)). The decrease in loading noise due to out-of-plane forces can be attributed to the reduction in lifting forces at the front of the rotor (see Fig. 14) and is discussed further below. Comparing the total noise contours in Fig. 15, the reduction in noise emissions occurs towards the front of the rotor due to reduction in loading noise there. While the quantitative effects of active-camber actuation on the acoustic footprint for 1P and 1P+2P cases from Fig. 10 are different, the qualitative effects are largely similar and are not presented here.

Figure 16 shows the acoustic noise corresponding to cases in Fig. 10 at locations A, B and C. The effect on total rotor noise essentially follows the trend of loading noise. Despite camber deflections of upto 8°, or changes to rotor tip-path plane due to changes in rotor trim angle from camber morphing, no significant variation in thickness noise were obtained. This can be seen from thickness noise OASPL-A results in Fig. 16(a) as well as from the acoustic pressure fluctuations from Figs. 16(b)-(d). Note that the scale of x-axes represents observer time for one blade passage and the thickness noise curves in Figs. 16(b)-(d) overlap one another given the scale of the figures. While some relative variations in thickness noise were obtained at location C, the corresponding influence on total noise is insignificant due to the logarithmic nature of the acoustic noise scale. As a result, any effect on rotor noise is entirely an outcome of changes in loading noise. Since changes in rotor lift forces are larger than drag forces, larger contributions of loading noise to total noise are seen at locations B and C below the rotor. In Fig. 16(d), the acoustic pressure fluctuation at location C due to loading forces is similar for 2P and the baseline case. Yet the differences in OASPL-A in Fig. 16(a) stem from different weightings for different frequencies. The unweighted OASPL for the 2P case is indeed the same as

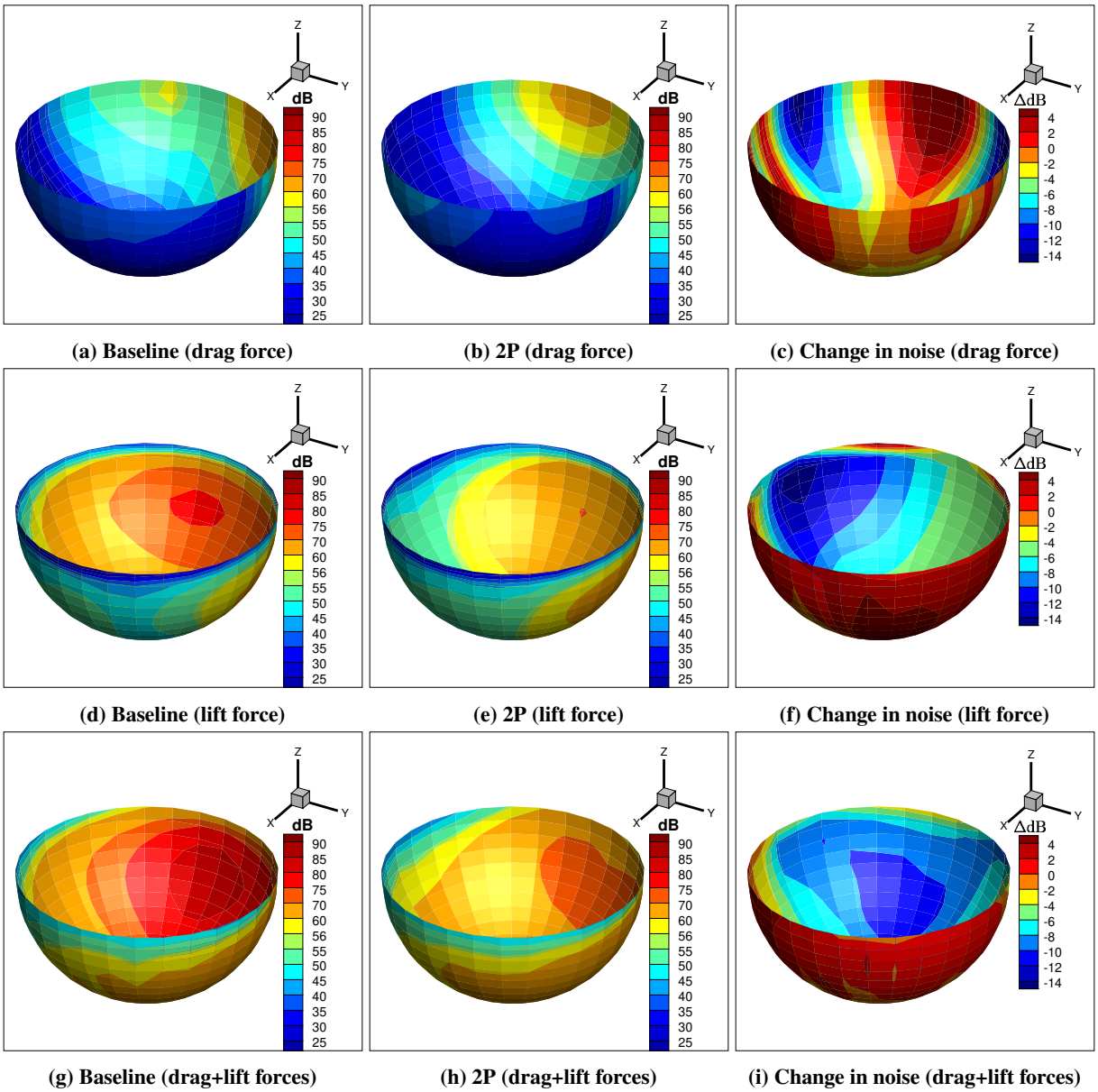

(a) Baseline (drag force) **(b) 2P (drag force)** **(c) Change in noise (drag force)**

(d) Baseline (lift force) **(e) 2P (lift force)** **(f) Change in noise (lift force)**

(g) Baseline (drag+lift forces) **(h) 2P (drag+lift forces)** **(i) Change in noise (drag+lift forces)**

Fig. 12 OASPL-A contours of loading noise for baseline rotor and 2P camber morphing case at μ=0.3 over a hemisphere of radius 50 m. (a)-(c) drag loading noise, (d)-(f) lift loading noise and (g)-(i) drag+lift loading noise.

the baseline case. The active rotor noise effects detailed above can be analyzed using the formulation of just the far-field noise -

$$4\pi p'_{\text{far}}(\mathbf{x},t) = \underbrace{\int_{f=0} \left[\frac{\rho_o \dot{v}_n}{r(1-M_r)^2}\right]_{\text{ret}} dS}_{\text{far-field thickness noise}} + \frac{1}{c}\underbrace{\int_{f=0} \left[\frac{\dot{l}_r}{r\,(1-M_r)^2}\right]_{\text{ret}} dS}_{\text{far-field loading noise}} \tag{5}$$

Equation 5 shows the terms from the integral solution in Eq. 3 that are predominant in the far-field i.e. terms with the lowest powers of r and $(1-M_r)$ in the denominator. Any attenuation of the effect of blade thickness noise would come from an 'anti-noise' pulse generated by a change in blade loading. Since the peak thickness noise occurs near the advancing side of the rotor (due to dominance of $(1-M_r)^2$ term in denominator), a signal of opposite sign near the advancing side due to change in blade loading could counter this effect. This idea was previously investigated both

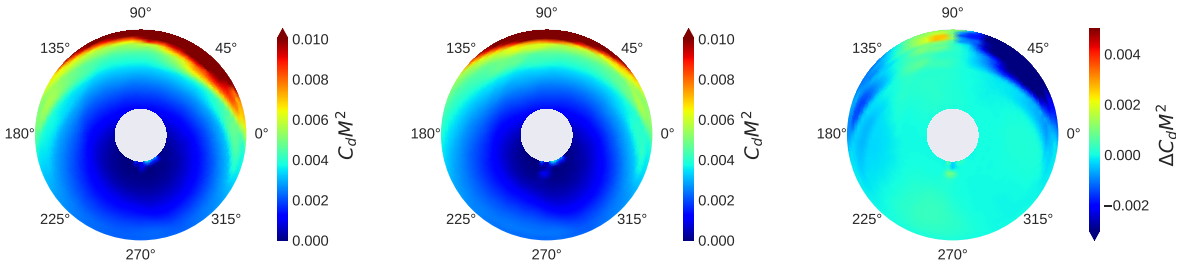

(a) Baseline **(b) 2P** **(c) Change in rotor drag**

Fig. 13 Azimuthal distribution of blade drag loads for the baseline rotor and 2P camber morphing case with best performance at μ=0.3.

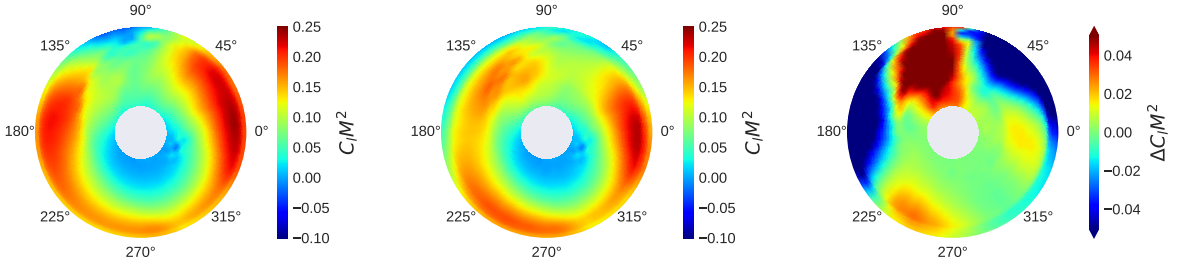

(a) Baseline **(b) 2P** **(c) Change in rotor lift**

Fig. 14 Azimuthal distribution of blade lifting loads for the baseline rotor and 2P camber morphing case with best performance at μ=0.3.

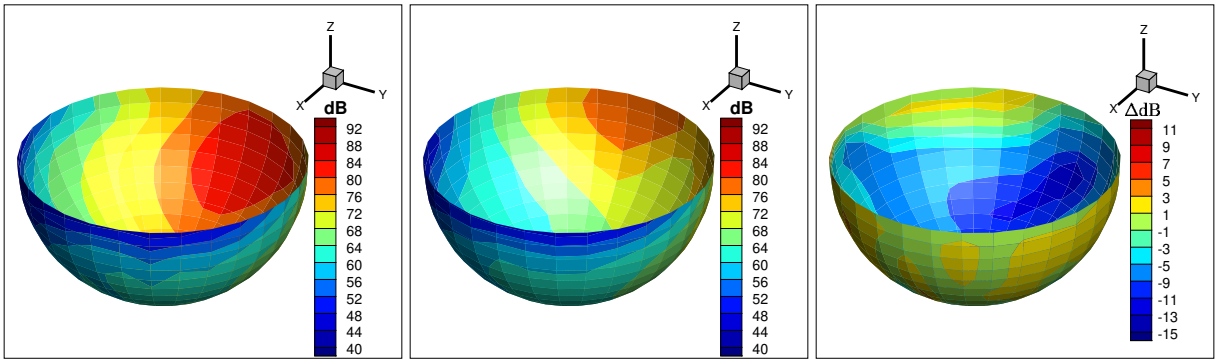

(a) Baseline **(b) 2P** **(c) Change in noise**

Fig. 15 OASPL-A contours of total noise for baseline rotor and 2P camber morphing case at μ=0.3 over a hemisphere of radius 50 m.

theoretically [5] and experimentally [6]. Considering the in-plane directivity and the pulsing character of thickness noise (see Fig. 16(b)), a pulsating increase in rotor drag ($\dot{l}_r > 0$) would be necessary to counter the characteristic negative thickness noise pulse. However, it can be seen from contour plots in Fig.13(c) that no large increase in blade drag was observed near $\psi = 90°$. As a result, the general character of thickness noise radiated from the active rotor remains the same as the baseline rotor. An increase in thrust loads, i.e. $\dot{l}_r > 0$, close to the azimuth of location B results in the increase in acoustic pressure seen for all active actuation cases in Fig. 16(c).

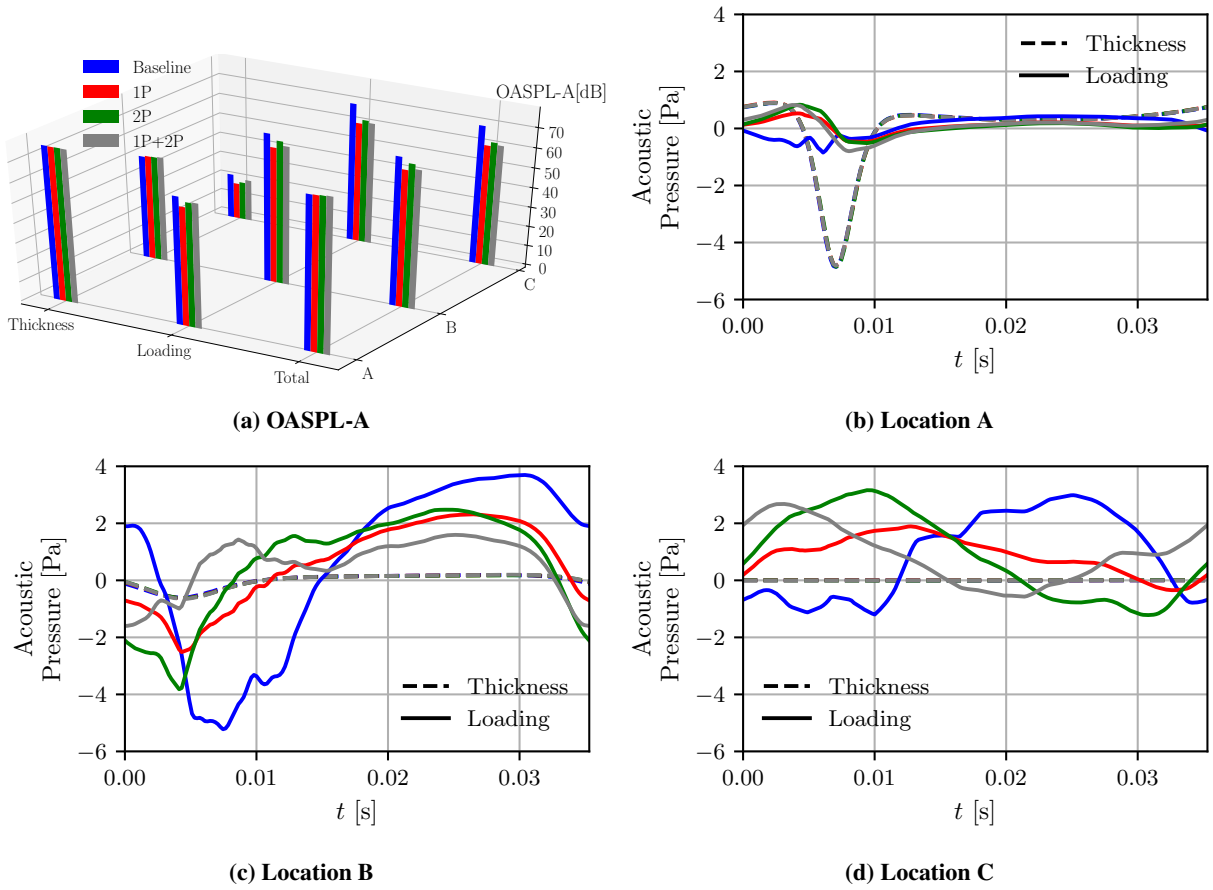

(a) OASPL-A **(b) Location A**

(c) Location B **(d) Location C**

Fig. 16 OASPL-A, and thickness and loading acoustic pressure results for the best performance cases at three representative observer locations with respect to the rotor plane. In-plane observer location A, out-of-plane observer location B, and observer location below the rotor hub C (see Fig. 6). See (a) for color coding.

V. Summary and Conclusions

A full-scale Bo 105 helicopter rotor with an active-camber morphing concept was investigated in this study. The objective was to quantify the effect of rotor camber morphing on the acoustic footprint, while simultaneously also investigating the effect on rotor power and induced hub vibration. CAMRAD II was used for the aeromechanical analysis and PSU-WOPWOP for analyzing rotor noise based on the trimmed rotor results. The investigation was carried out for a sweep of advance ratios ranging from $\mu = 0.05$ to $\mu = 0.35$, phase angles of $0° - 360°$, and different amplitudes for 1P and 2P actuation frequencies. This parameter design space provided a good overview of the effects of active-camber actuation on rotor noise, performance (in terms of C_P) and hub vibration (in terms of J), at a given operating condition. A post-processing framework was developed in Python to generate the blade geometry and the relevant input files required by the acoustics solver using CAMRAD II aeromechanics output. This framework is publicly available at `https://github.com/kumar-sumeet/helinoise.git`.

Based on the study, the following conclusions can be made:

- Performance improvement was obtained, in general, by decreasing thrust over sections of the baseline rotor disk where it was high and increasing it where it was low. For low advance ratios this meant off-loading the rotor tips everywhere over the rotor azimuth, and increasing loading inboard, i.e. redistributing the thrust more uniformly. This was accomplished using a constant camber deflection component δ_0 rather than actuation amplitude A_{mP} within the deflection profile.
- For higher advance ratios it was the fore and aft sections of the rotor disk that were off-loaded and loading was increased on the advancing and retreating sides. This was achieved only with limited active-camber deflection

phase inputs. For 2P actuation, the hub vibration index was always higher for these phase inputs, so simultaneous reduction in hub vibration and rotor power was not obtained. Similar results were obtained for 1P actuation as well, except that few cases showed both power and vibration reduction for $\mu = 0.35$.

- Simultaneous reduction in rotor noise at an out-of-plane observer location and power consumption was obtained at all advanced ratios ($\mu = 0.05 - 0.35$) investigated and for both 1P and 2P actuation.
- Overall, active-camber morphing reduced rotor noise, power, and hub vibration simultaneously for low advance ratio μ =0.10 and 0.15. For these cases, it was possible to choose suitable amplitude (A_{mP}) and phase inputs such that vibration index (J) was also reduced, while having limited effect on corresponding performance improvement as long as δ_0 was non-zero. Similar effects on rotor performance (C_P) and and hub vibration (J) were also obtained at $\mu = 0.05$ but noise was always increased for these cases at the out-of-plane observer location B considered in this study. Since the trim conditions were chosen such that no blade–vortex interaction occured at low advance ratios, any changes in rotor noise were entirely attributed to changes in thrust distribution over the rotor disk.
- Most thrust distributions that resulted in performance improvement also resulted in noise reduction. This trend was obtained for all advance ratios ($\mu = 0.05 - 0.35$). Consequently, simultaneous noise and power reduction was possible for all advance ratios using active-camber morphing.
- Blade section deformation due to active-camber morphing or any change in blade tip-path plane due to change in trim control angles did not significantly influence blade thickness noise. As a result any changes in in-plane noise were small and due to change in blade drag over the rotor disk.

While power consumption is a unique parameter of the rotor, induced hub vibrations depend on the metric used to define it. For different camber actuation phases, the 4P hub forces and moments are affected differently, and using suitable weightings between them can certainly alter the trends observed for the vibration index, J. Likewise, rotor noise at a given observer location is a characteristic of the time-history of the rotor geometry and the blade airloads. However, the changes in rotor noise due to camber actuation are different at different observer locations. In the current study only three observer locations that were most affected by noise changes due to active-camber were investigated.

Acknowledgements

This work was carried out within the SABRE project that has received funding from the European Union's Horizon 2020 research and innovation program under grant agreement No. 723491.

References

[1] van der Wall, B. G., Kessler, C., Delrieux, Y., Beaumier, P., Gervais, M., Hirsch, J., Pengel, K., and Crozier, P., "From ERATO Basic Research to the Blue Edge$^{\mathrm{TM}}$ Rotor Blade," *American Helicopter Society 72nd Annual Forum, West Palm Beach, Florida*, 2016.

[2] Brentner, K. S., Edwards, B. D., Riley, R., and Schillings, J., "Predicted noise for a main rotor with modulated blade spacing," *Journal of the American Helicopter Society*, Vol. 50, No. 1, 2005, pp. 18–25. https://doi.org/10.4050/1.3092839.

[3] Sullivan, B. M., Edwards, B. D., Brentner, K. S., and Booth, E. R., "A subjective test of modulated blade spacing for helicopter main rotors," *Journal of the American Helicopter Society*, Vol. 50, No. 1, 2005, pp. 26–32. https://doi.org/10.4050/1.3092840.

[4] Schmitz, F. H., "Reduction of Blade-Vortex Interaction (BVI) Noise through X-Force Control," *Journal of the American Helicopter Society*, Vol. 43, No. 1, 1998, pp. 14–24. https://doi.org/10.4050/JAHS.43.14.

[5] Gopalan, G., and Schmitz, F. H., "Helicopter Thickness Noise Reduction Possibilities Through Active On-Blade Acoustic Control," *Journal of Aircraft*, Vol. 47, No. 1, 2010, pp. 41–52. https://doi.org/10.2514/1.35695.

[6] Sim, B. W., JanakiRam, R. D., and Lau, B. H., "Reduced In-Plane, Low-Frequency Noise of an Active Flap Rotor," *Journal of the American Helicopter Society*, Vol. 59, No. 2, 2014. https://doi.org/10.4050/JAHS.59.022002.

[7] Yang, T., Brentner, K. S., Corle, E., and Schmitz, S., "Study of Active Rotor Control for In-Plane Rotor Noise Reduction," *Journal of Aircraft*, Vol. 56, No. 1, 2019, pp. 179–190. https://doi.org/10.2514/1.C034873.

[8] Komp, D., Kumar, S., Hajek, M., and Rauleder, J., "Effect of Active Camber Morphing on Rotor Performance and Control Loads," *Aerospace Science and Technology*, 2020. https://doi.org/10.1016/j.ast.2020.106311.

[9] Kumar, S., Komp, D., Hajek, M., and Rauleder, J., "Integrated Rotor Performance Improvement and Vibration Reduction Using Active Camber Morphing," *ASME Conference on Smart Materials, Adaptive Structures and Intelligent Systems*, 2019. https://doi.org/10.1115/SMASIS2019-5588.

[10] Johnson, W., "Technology Drivers in the Development of CAMRAD II," *American Helicopter Society Aeromechanics Specialists Conference*, 1994.

[11] Shirey, J., Brentner, K., and Chen, H.-n., "A Validation Study of the PSU-WOPWOP Rotor Noise Prediction Code," *45th AIAA Aerospace Sciences Meeting and Exhibit*, Reno,NV, 2007. https://doi.org/10.2514/6.2007-1240.

[12] Abdelmoula, A., and Rauleder, J., "Aerodynamic performance of morphed camber rotor airfoils," *AIAA Scitech 2019 Forum*, 2019. https://doi.org/10.2514/6.2019-1101.

[13] Komp, D., Hajek, M., and Rauleder, J., "Rotor Performance Enhancements with Spanwise Varying Active Camber Morphing," *AIAA SciTech Forum*, 202a.

[14] Komp, D., Kumar, S., Abdelmoula, A., Hajek, M., and Rauleder, J., "Investigation of Active Rotor Design and Control for Performance Improvement," *Vertical Flight Society 75th Annual Forum, Philadelphia, PA*, 2019.

[15] Farassat, F., and Succi, G. P., "A review of propeller discrete frequency noise prediction technology with emphasis on two current methods for time domain calculations," *Journal of Sound and Vibration*, Vol. 71, No. 3, 1980, pp. 399–419. https://doi.org/10.1016/0022-460X(80)90422-8.

[16] Schmitz, F. H., "Rotor Noise," *Aeroacoustics of Flight Vehicles, Theory and Practice, Vol. 1: Noise Sources*, edited by H. H. Hubbard, NASA TR 90-3052, 1991, Chap. 2.

[17] Pflumm, T., Garre, W., and Hajek, M., "A Preprocessor for Parametric Composite Rotor Blade Cross-Sections," *44th European Rotocraft Forum, Delft, The Netherlands*, 2018.

[18] Hennes, C., Lopes, L., Shirey, J., Erwin, J., Goldman, B. A., and Brentner, K. S., "PSU-WOPWOP 3.4.3 User's Guide," *The Pennsylvania State University, University Park, PA*, 2015.

[19] Bauchau, O. A., "DYMORE User's Manual," *Georgia Institute of Technology, Atlanta*, 2007.

[20] Schwamborn, D., Gardner, A. D., von Geyr, H., Krumbein, A., Lüdeke, H., and Stürmer, A., "Development of the DLR TAU-code for Aerospace Applications," *International Conference on Aerospace Science and Technology, Bangalore, India*, 2008.

[21] Özkurt, S., Fichter, W., Rath, T., Dieterich, O., Priems, M., Bülthoff, H., and Nooij, S., "From Helicopter Vibrations to Passenger Perceptions: A Closer Look on Standards," *76th Annual Forum & Technology Display of the Vertical Flight Society*, 2020.

[22] Delfs, J., *Grundlagen der Aeroakustik (Basics of Aeroacoustics)*, Technische Universität Braunschweig, Braunschweig, 2016.